Tailored biomimetic nanoreactor improves glioma chemodynamic treatment via triple glutathione depletion and prompt acidity elevation

Ya Wen [a,1] , Qiansai Qiu [b,1] , Feng Feng [b,1] , Yujuan Zhu [a] , Jianquan Zhang [b] , Zesheng Sun [a] , Tuodi Zhang [a] , Wei Shi [a] , Jinlong Shi [a,*]

[a] Department of Neurosurgery, Research Center of Clinical Medicine, Affiliated Hospital of Nantong University, Nantong University, Nantong, 226001, China
[b] Department of Radiology, Tumor Hospital Affiliated to Nantong University, Nantong, 226001, China

ARTICLE INFO

ABSTRACT

Chemodynamic therapy (CDT) is an emerging antitumor strategy utilizing iron-initiated Fenton reaction to destroy tumor cells by converting endogenous H_2O_2 into highly toxic hydroxyl radical (OH). However, the intratumoral overexpressed glutathione (GSH) and deficient acid greatly reduce CDT efficacy because of OH scavenging and decreased OH production efficiency. Even worse, the various physiological barriers, especially in glioma, further put the brakes on the targeted delivery of Fenton agents. Herein, by exploring the thiol reaction potential of 5,5′-dithiobis-2-nitrobenzoic acid (DTNB), we have constructed a tailored biomimetic nanoreactor to improve glioma CDT efficacy through synchronous GSH exhaustion and acidity elevation. The biomimetic nanoreactor was fabricated by employing DTNB to drive the nano-assembly of BSA molecules, followed by loading the carrier onto the cell surface of neutrophils via disulfide-thiol exchange. Upon sensing the inflammatory signal, the nanoreactor hijacked by neutrophils efficiently targets to the tumor site, which then dually depletes GSH by disulfide bond stabilizing the nanostructure and the following liberated Fe (III). In particular, the simultaneously released DTNB can not only consume the residual GSH, but also produce 5-thio-2-nitrobenzoic acid (TNB) promptly, resulting in accelerated Fenton reaction. Through *in vitro* and *in vivo* experiments, we demonstrate the exhaustive and synchronous regulation of Fenton chemistry could potentially serve as a novel CDT strategy for glioma.

1. Introduction

In emerging nano-catalytic medicine, chemodynamic therapy (CDT), as a novel therapeutic alternative to tumors, has attracted increasing research attention owing to the potent cytotoxicity of hydroxyl radical (·OH) boosted by Fenton reactions [1,2]. Owing to the distinctive mechanism of intratumoral manipulation, CDT is supposed to precisely target and eliminate cancer cells while being blind to normal tissues, rendering it the improved tumor specificity and reduced systemic toxicity [3]. More importantly, CDT needs no further field stimulation during the course of treatment, thereby avoiding the penetration/biosafety-related issues. However, despite the advantages presented, CDT still suffers from low therapeutic performance [4]. On one hand, the efficacy of CDT mainly relies on the concentration of toxic ·OH produced by Fenton reaction, which is energetic in an acid condition (pH ≈ 2–4) [5]. Nevertheless, the existed antioxidant system and

deficient acidity could severely impede the effective implementation of CDT [6,7]. On the other hand, due to the various physiological barriers, especially the blood-brain barrier (BBB) and blood-tumor barrier (BTB) in glioma, the deposition of Fenton agents is greatly compromised by the nanoparticle-based drug delivery systems [8,9], which fundamentally limits the outcome of CDT.

Through scavenging the stock and inhibiting the production of intracellular ·OH, the robust antioxidant system and weak acid environment constitute the two complementary factors responsible for the poor efficacy of CDT. Among the various antioxidant substances, glutathione (GSH) is regarded as the most predominant antioxidant system, enabling the reduction of GSH concentration to be a potent strategy for ·OH enrichment [10–12]. Compared with the suppression of GSH synthesis or regeneration, directly consuming GSH reserves represents a rapid and effective manner to decrease the intracellular GSH levels [13]. In this regard, numerous GSH-responsive Fenton nanoagents

comprising manganese dioxide, Fe (III), Cu (II), disulfides or oxidation state molecule have been reported to boost Fenton reaction [13–15]. However, on account of the insufficient depletion of GSH by single approach and the hypersensitivity of ·OH to residual GSH, CDT alone can barely eliminate malignant tumors and therefore needs combined therapy [16]. Apart from overexpressed GSH, the deficient acid of tumor milieu (pH ≈ 6.5) imposes another adverse factor on CDT through decreasing the production efficiency of ·OH [17–19]. Recently, attempts have been made to address this issue by customizing the tumor milieu through in situ H^+ generation or acidosis reconstruction. Glucose oxidase can catalyze glucose oxidation into gluconic acid [20,21], therefore being widely employed to reinforce the efficiency of Fenton reaction. Beyond that, the overexpressed carbonic anhydrase IX (CA IX) is known to play important roles in maintaining the weak acid pH of cytosol [22], thus inhibiting the activity of CA IX enzyme shows another approach to re-establish tumor acidosis and accelerate the ·OH production. Nevertheless, besides the insufficient H^+ yield, these strategies take a long time to acidize the tumor milieu [5], which generally mismatches with the rapidly occurred Fenton reaction. Therefore, it is reasonable to combine the sufficient GSH depletion and prompt acidity elevation for effective implementation of CDT.

Unfortunately, the targeted deposition of Fenton agents, as the precondition for the fulfillment of CDT, by nano-system is often hindered because of the BBB/BTB and dense extracellular matrix in glioma [23]. Vectorization of therapeutics employing endogenous cells such as neutrophils (NEs), which possess inflammatory sensing ability to traverse physiological barriers [24–26], has recently been proposed as a potent targeting strategy for brain drug delivery. Generally, intracellular loading or cell surface attaching of therapeutics are widely utilized approaches to exploit the delivery capability of endogenous cells. Besides the limitation of cell types with phagocytosis capability, nanodrugs loaded in host cells may suffer from undesired degradation and release [27,28], which in turn may affect the cell targeting abilities. In contrast, attaching cargos on the cell surface is able to reduce the potential cytotoxicity and avoid the premature degradation, thus highly promising for drug targeted delivery. Generally, nanodrugs can be loaded on cell surface via charge-dependent adsorption, ligand-receptor attachment, and covalent coupling [29,30]. However, these approaches possess inherent drawbacks [31]: charge-dependent adsorption is likely instable, ligand-receptor attachment may interfere the signal transduction, while the covalent coupling is usually manipulated in harsh conditions and accompanied by unloading concerns. It is therefore essential to seek alternative method with simplicity, cytocompatibility and reversibility to improve the targeting efficiency of Fenton agents.

In previous works [32,33], we demonstrated, in an efficient and cytocompatible manner, 5,5′-dithiobis-2-nitrobenzoic acid (DTNB) is able to drive the disulfide crosslink of protein nanoparticles onto cell surface through disulfide-thiol exchange for its efficient leaving group of 5-thio-2-nitrobenzoic acid (TNB). Given the cleavable property of the interfacial disulfide, it is appealing to explore its potential in nanodrug loading application. More importantly, if delicately used as an oxidant, DTNB can not only fast deplete the intracellular GSH, but also acidize the tumor milieu synchronously by side product TNB, indicating the regulation potential for Fenton chemistry. Therefore, in this study, by exploring the thiol reaction capacity of DTNB, we report a tailored biomimetic nanoreactor to improve glioma CDT efficacy through synchronous GSH exhaustion and acidity elevation (Scheme 1). To obtain the biomimetic nanoreactor (DTNB/Fe(III)@BNP-NEs), DTNB and Fe (III) are encapsulated into the bovine serum albumin (BSA) nanoparticles (BNP) stabilized with disulfide network, followed by loading onto the surface of NEs via disulfide-thiol exchange (Fig. S1). Upon sensing the inflammatory signal, the nanoreactor DTNB/Fe(III)@BNP hijacked by NEs efficiently targets to the tumor site, wherein DTNB/Fe (III)@BNP is unloaded in response to the enzymes or other reducing substances released by the over-activated NEs. Once being internalized, DTNB/Fe(III)@BNP triply depletes the intracellular GSH and promptly elevates the acidity of tumor milieu through disulfides and the subsequent liberated Fe (III) and DTNB, leading to enhanced Fenton reaction efficacy. Based on *in vitro* and *in vivo* results, we proved such exhaustive and synchronous regulation of Fenton chemistry could potentially serve as a novel CDT strategy for glioma.

2. Results and discussion

Preparation and Characterization of Nanoreactor. The nanoreactor DTNB/Fe(III)@BNP was synthesized by exploiting the reaction
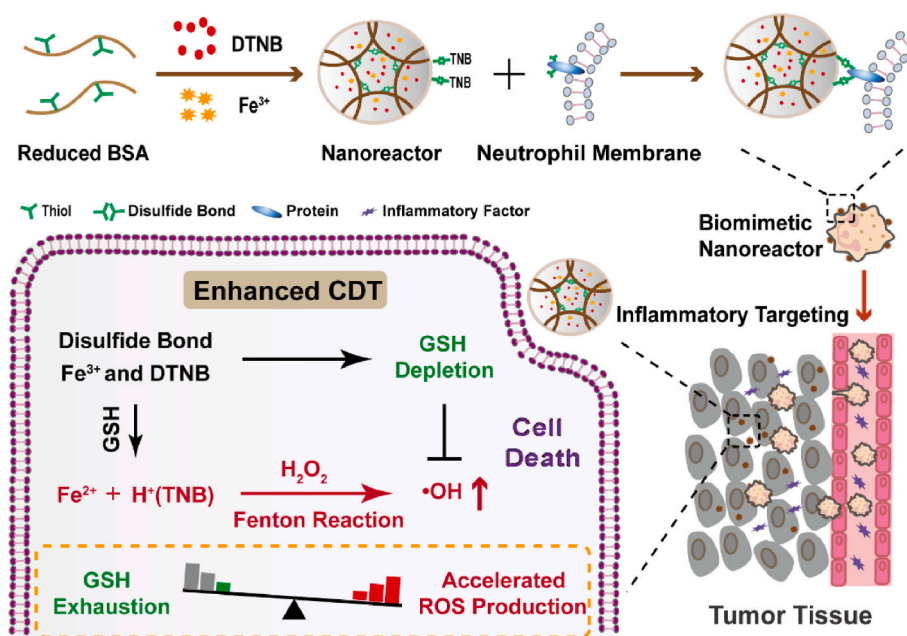
Scheme 1. Schematic illustration of biomimetic nanoreactor for glioma chemodynamic therapy (CDT) through synchronous GSH exhaustion and acidity elevation. Upon sensing the inflammatory signal, the nanoreactor hijacked by NEs efficiently targets to the tumor site, which triply depletes the intracellular GSH and promptly acidizes the tumor milieu, leading to enhanced Fenton reaction efficacy for glioma CDT.

ability of DTNB against thiols in BSA. Briefly, BSA was firstly reduced by dithiothreitol (DTT) to obtain the reduced BSA (rBSA), which were then activated by excessive DTNB under rigorous stirring. Subsequently, equivalent rBSA along with the Fenton agent Fe (III) was introduced to drive the intermolecular disulfide crosslinking of BSA as well as the drug loading, the nanoreactor DTNB/Fe(III)@BNP was thus obtained with loading contents of 7.12 % and 0.33 % to DTNB and Fe(III), respectively.

DTNB/Fe(III)@BNP exhibits a spherical morphology with narrow size distribution as shown in Fig. 1a. Since the stability is very important for *in vivo* application, DTNB/Fe(III)@BNP was dispersed in DMEM containing 10 % FBS mimicking the physiological environment and the size was measured at predetermined time points. As shown in Fig. 1b, DTNB/Fe(III)@BNP showed negligible size variation after 7 day incubation, implying the stable property of the nanoreactor. To elucidate the forces that stabilized the nanostructure, sodium dodecyl sulfate (SDS), ethylene diamine tetraacetic acid (EDTA) and DTT were introduced as destroyers of hydrophobicity, chelation and disulfide respectively into DTNB/Fe(III)@BNP solution. As shown in Fig. S2, SDS and EDTA could cause the variation of particle size, while DTT almost dissociated the nanoparticle since the size of DTNB/Fe(III)@BNP suffered significant decrease. This implies though physical forces existed, disulfide crosslink

dominated the forces stabilizing the nanreactor. To further validate the existence of disulfide, DTNB/Fe(III)@BNP was incubated with GSH (10 mM), and decreased particle size was observed (Fig. 1c and Fig. S3). Moreover, X-ray photoelectron spectroscopy (XPS) was also utilized to verify the formation of disulfide. As shown in Fig. S4, the S 2p peak of DTNB/Fe(III)@BNP located at 163.5 eV, which was associated with the presence of disulfide, increased compared with that of rBSA. These results collectively validated the formation of disulfide network which endowed the nanoreactor with GSH-cleavage and depletion property. As expected, DTNB/Fe(III)@BNP showed accelerated DTNB release in the presence of GSH supplementation (Fig. 1d). The cumulative released DTNB was calculated by addition of the depleted (TNB) and free DTNB in the presence of GSH (Fig. S5).

As DTNB continuously liberated from DTNB/Fe(III)@BNP upon GSH treatment, pH of the solution dramatically decreased due to the presence of acidic TNB generated from GSH depletion by DTNB (Fig. 1e), indicating the capacity of DTNB/Fe(III)@BNP for acidifying tumor milieu. To detect the ·OH generation under simulated normal and acidized tumor milieu boosted by Fe-initiated Fenton reaction, rhodamine B (RhB) was used as the ROS indicator and added into DTNB/Fe(III)@BNP following the sequential introduction of GSH and H_2O_2. Intriguing, as
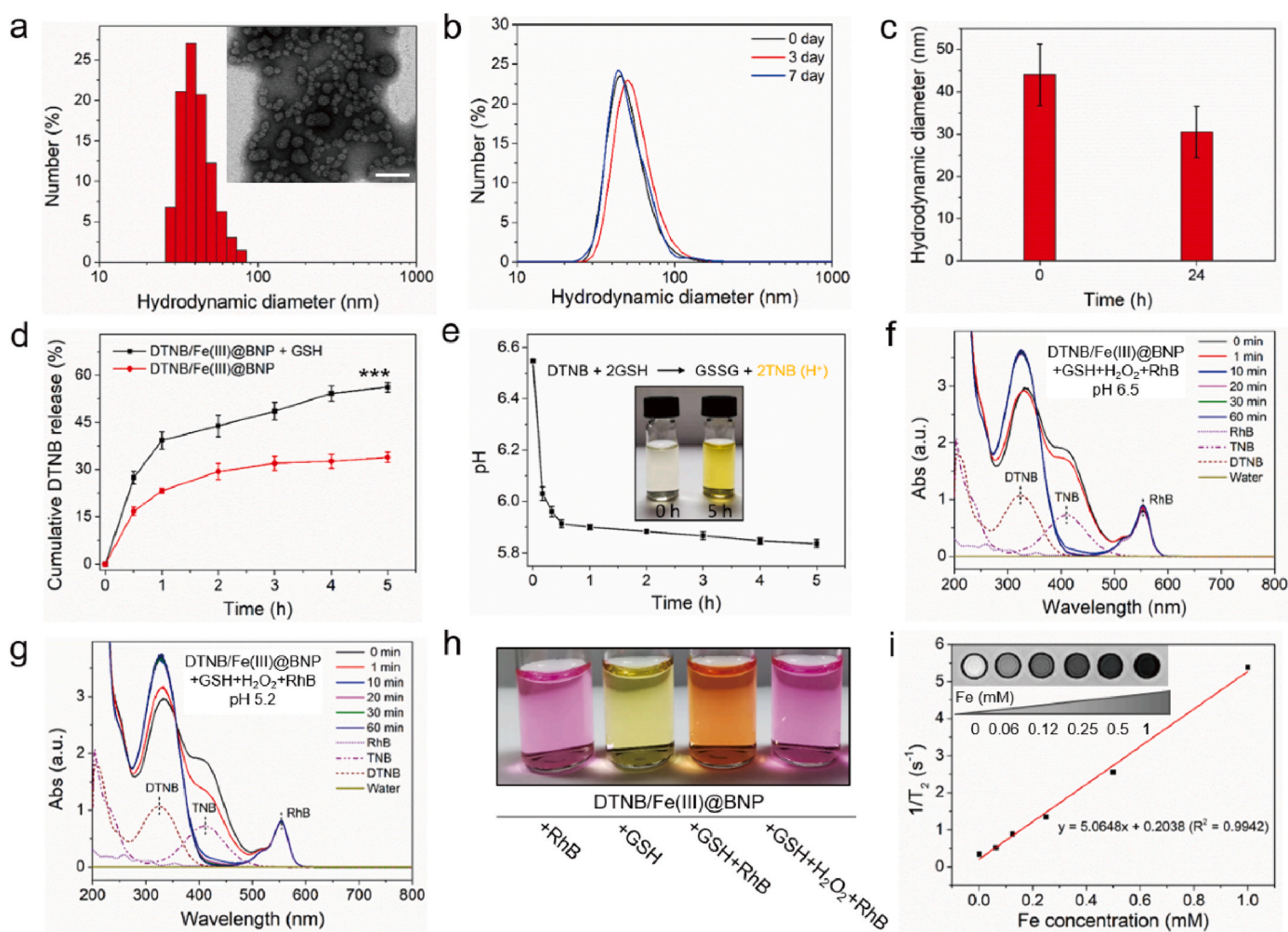

Fig. 1. Preparation and characterization of nanoreactor. (a) Particle size distribution of DTNB/Fe(III)@BNP determined by dynamic light scattering. Inset: transmission electronic microscope image of DTNB/Fe(III)@BNP. 100 nm in the legend. (b) Stability of DTNB/Fe(III)@BNP in DMEM containing 10 % FBS. (c) Hydrodynamic diameter of DTNB/Fe(III)@BNP subjected to 10 mM GSH treatment ($n = 3$). (d) Cumulative DTNB release profile of DTNB/Fe(III)@BNP in the presence or absence of 10 mM GSH ($n = 3$). ***$P < 0.001$. (e) pH of DTNB/Fe(III)@BNP upon treatment with 10 mM GSH ($n = 3$). (f) Detection of ·OH production from DTNB/Fe(III)@BNP pretreated with 1 mM GSH for 3 h followed by introduction of 1 mM H_2O_2 by measuring TNB and rhodamine B (RhB) absorbance at pH 6.5 and (g) pH 5.2. (h) Optical photographs of different mixed solutions at 1 h post sequential addition of GSH or H_2O_2. (i) Plots of T_2^{-1} against Fe concentration and Fe-mediated MR imaging of DTNB/Fe(III)@BNP.

shown in Fig. 1f and g, the absorbance of RhB was found no apparent changes, while significant decrease of TNB and corresponding increase of DTNB in absorbance were observed, and the reciprocal transformation was more drastic in the lower pH condition. In contrast, no absorbance changes were detected after the treatment only in the presence of GSH or H_2O_2 (Fig. S6). These results suggested TNB probably had stronger reduction ability than RhB and could be preferentially oxidized to DTNB, which could be further accelerated in acidized condition, indicating the effective ·OH production ability of DTNB/Fe(III) @BNP through Fenton reaction. Fig. 1h showed the optical photographs of different mixed solutions after sequential addition of GSH or H_2O_2, the color changes of which were consistent with the above results. In addition, as shown in Fig. 1i, intensity (darkness) of T2-weighted MRI of DTNB/Fe(III)@BNP was gradually enhanced and the corresponding relaxation rate ($1/T_2$) was varied linearly as Fe concentration increased. The results indicated that Fe (III) loading enabled DTNB/Fe(III)@BNP to be a favorable T2-weighted MR contrast agent, with r_2 relaxation (slope of the curve) value of 5.0648 mM^{-1} s^{-1}.

Boosted Fenton Reaction Efficiency by Synchronous GSH Exhaustion and Acidity Elevation. To examine the cytotoxicity of DTNB/Fe(III)@BNP on C6 cells, CCK-8 assay was performed. For comparison, BNP and Fe(III)@BNP with similar size (Fig. S7) were also synthesized and used as controls. As shown in Fig. 2a, all nanoformulations exhibited concentration-dependent toxicity, whereas Fe (III)@BNP and DTNB/Fe(III)@BNP presented gradually improved cell killing effect after internalization (Fig. S8) compared with BNP. The apoptosis analysis was consistent with the CCK-8 results (Fig. 2b). This was presumably attributed to the multiple regulation of intracellular Fenton chemistry involving the sufficient GSH depletion and prompt acidity elevation. Interestingly, Fenton agents Fe (III) and membrane-impermeable DTNB alone used enhanced the cell propagation, probably due to their multiple roles in cell metabolism, which underlined the necessity of integration for achieving favorable Fenton reaction performance.

To verify our speculation on enhanced cytotoxicity of the nanoreactor, the regulation property for intracellular Fenton chemistry was examined. As shown in Fig. 2c and Table S1, the three nanoformulations all induced GSH depletion in a kinetic manner, while at
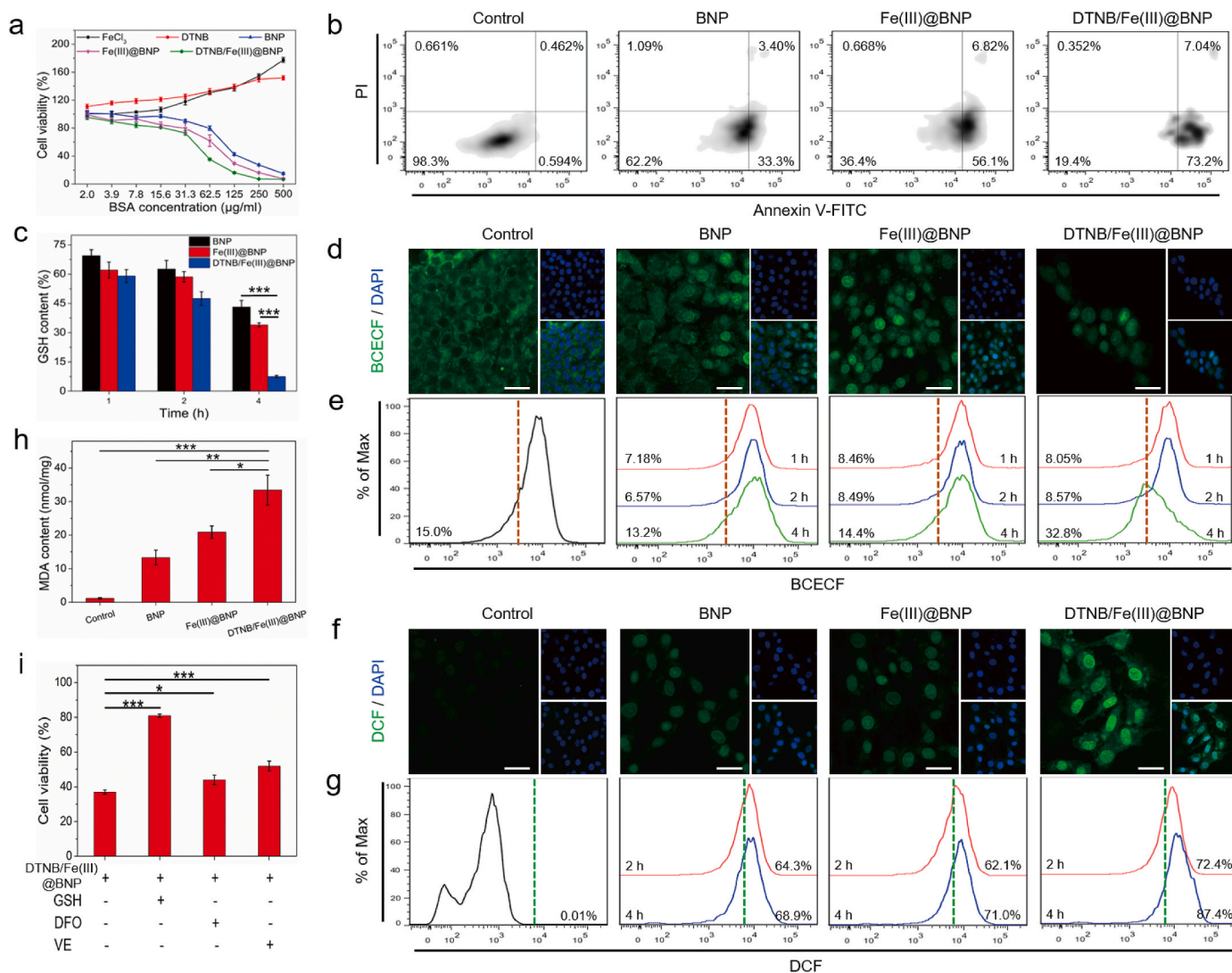

Fig. 2. Fenton reaction induced cytotoxicity of the nanoreactor is boosted by synchronous GSH exhaustion and acidity elevation. (a) Viability and (b) apoptosis of C6 cells in response to BNP, Fe(III)@BNP and DTNB/Fe(III)@BNP treatment. The dosage of free FeCl₃ and DTNB were equivalent to that of DTNB/Fe(III)@BNP. (c) The intracellular GSH depletion, (d, e) acidity elevation and (f, g) ·OH production of C6 cells at different time points after BNP, Fe(III)@BNP and DTNB/Fe(III)@BNP treatment. Scale bar, 20 μm ***$P < 0.001$. (h) Malonaldehyde (MDA) content of C6 cells treated with BNP, Fe(III)@BNP and DTNB/Fe(III)@BNP for 4 h ($n = 3$). *$P < 0.05$, **$P < 0.01$, ***$P < 0.001$. (i) Viability of C6 cells in response to DTNB/Fe(III)@BNP followed by the replacement with Fenton reaction inhibitors, including 5 mM GSH, 100 μM deferoxamine (DFO), and 100 μM vitamin E (VE). *$P < 0.05$, ***$P < 0.001$.

each time point, BNP, Fe(III)@BNP and DTNB/Fe(III)@BNP exhibited gradually increased consumption on intracellular GSH. This is fully matched with the single, dual or triple GSH depletion strategy imposed on BNP, Fe(III)@BNP and DTNB/Fe(III)@BNP through disulfide and the released cargoes, indicating the potential of nanoreactor for GSH exhaustion. Once liberated, DTNB rapidly reacted with GSH and produced acidic TNB, which is of vital importance for the efficient occurrence of Fenton reaction. To detect the change of intracellular acidity, 2′,7′-bis-(2-carboxyethyl)-5-(and-6)-carboxyfluorescein, acetoxymethyl ester (BCECF-AM), a fluorescent pH probe, was employed. As expected (Fig. 2e), DTNB/Fe(III)@BNP caused the obvious acidity elevation since the fluorescence signal of BCECF dramatically decreased after 4 h incubation, a time dimension in accordance with the GSH exhaustion. In contrast, neither BNP nor Fe(III)@BNP induced apparent acidity variation, indicating the significant role of DTNB in acidifying the intracellular environment. The acidity change was also visualized using confocal laser scanning microscope (CLSM) (Fig. 2d), in which the BCECF signal could barely observed in the cytoplasm of DTNB/Fe(III)@BNP treated cells, in sharp contrast with that of the control, BNP and Fe(III)@BNP groups. This result was well consistent with the flow analysis and showed the prompt acidity elevation capability of DTNB/Fe(III)@BNP. Upon synchronous GSH exhaustion and acidity elevation,

Fenton reaction is supposed to proceed efficiently, we thus measured the ·OH production using ROS indicator 2′,7′-dichlorofluorescin diacetate (DCFH-DA). As shown in Fig. 2g, significantly increased fluorescence signal of DCF was found in response to DTNB/Fe(III)@BNP treatment, whereas BNP and Fe(III)@BNP groups presented apparently lower fluorescence intensity, which was mainly ascribed to the insufficient GSH depletion and deficient intracellular acidity. The ·OH production of DTNB/Fe(III)@BNP was further confirmed by CLSM investigation (Fig. 2f), which was in agreement with the flow analysis, indicating the efficient regulation property of intracellular Fenton chemistry.

Since excess ROS can induce the lipid peroxidation of cell membrane, the marker of this process, malonaldehyde (MDA), were quantitatively evaluated to further verify the production of ·OH. As shown in Fig. 2h, DTNB/Fe(III)@BNP treatment could significantly increase the intracellular MDA level compared with the other groups, validating the enhanced production of ·OH through efficient regulation of Fenton chemistry for cell killing. We further conducted a rescue experiment using GSH, deferoxamine (DFO), and vitamin E (VE) as the Fenton reaction inhibitors, given the antioxidative roles of GSH and VE as well as the iron chelation property of DFO [34]. The impaired cell viability significantly restored upon the subsequent incubation of the specific inhibitors (Fig. 2i), verifying the Fenton reaction induced cytotoxicity.
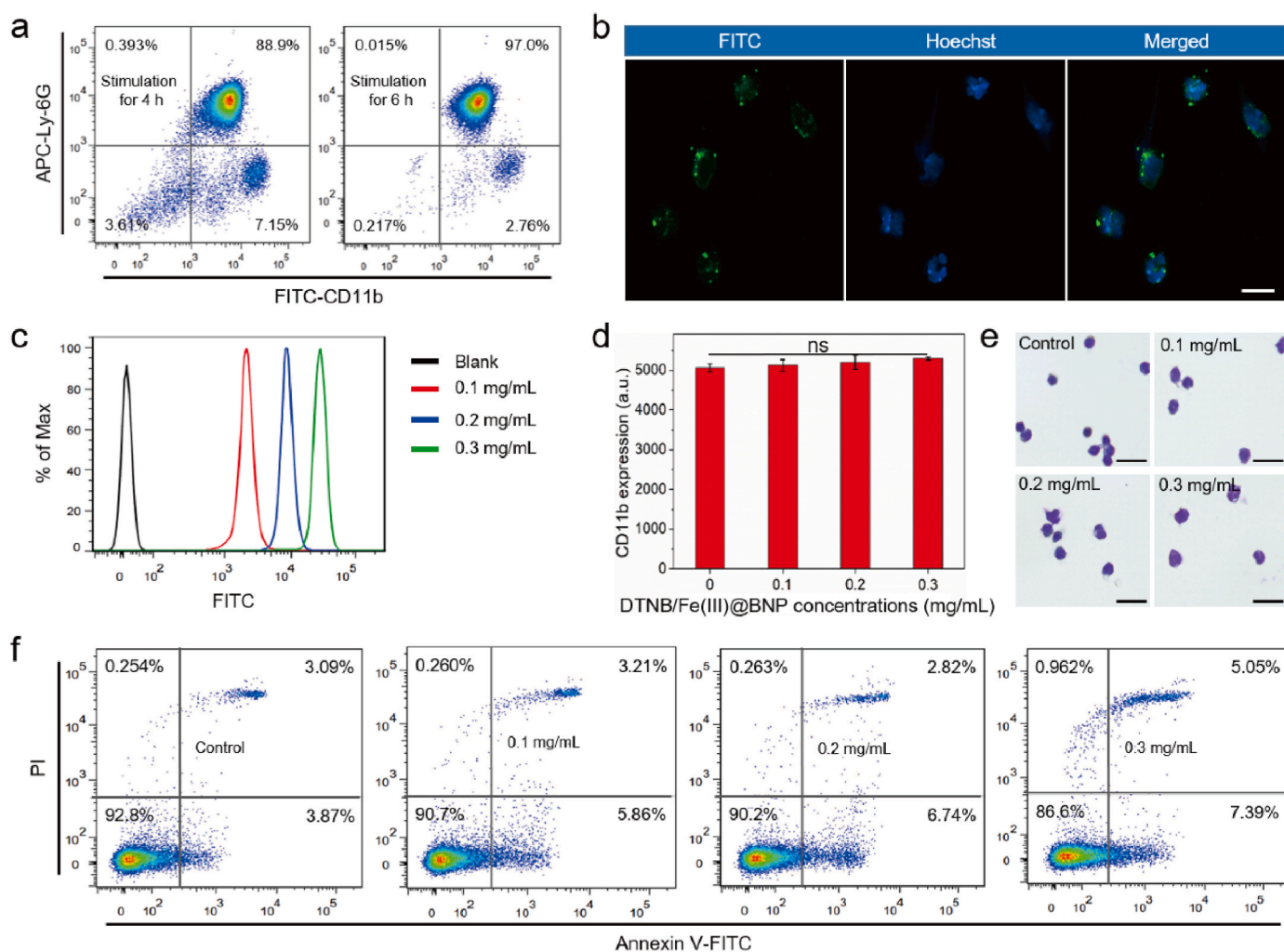

Fig. 3. Nanoreactor cell surface loading and characterization. (a) Purity analysis of NEs by flow cytometry. FITC-conjugated CD11b and APC-conjugated Ly-6G antibodies were utilized to stain the NEs. (b) CLSM images of NEs after DTNB/Fe(III)@BNP cell surface loading. Green fluorescence represents FITC-labeled DTNB/Fe (III)@BNP. Blue fluorescence represents polymorphonuclear of NEs stained with Hoechst. Scale bar, 10 μm. (c) Flow cytometry analysis of NEs treated with DTNB/Fe (III)@BNP at different concentrations. (d) CD11b expression of NEs after the treatment with various concentrations of DTNB/Fe(III)@BNP. ns: not significant. (e) Morphological visualization of NEs treated with different concentrations of DTNB/Fe(III)@BNP. Scale bar, 20 μm. (f) Apoptosis analysis of NEs in response to the treatment of DTNB/Fe(III)@BNP with different concentrations.

Taken together, these results demonstrated the synchronous GSH exhaustion and acidity elevation laid the foundation for boosted Fenton reaction efficiency, implying the potential application of the nanoreactor for glioma CDT.

Nanoreactor Cell Surface Loading and Characterization. The NEs were collected from inflammatory murine peritoneal cavity stimulated with thioglycollate broth, referred to the previous reported method. Since NEs can rapidly respond to the inflammatory stimuli, we further screened the time period for collecting NEs after the injection of thioglycollate broth. As shown in Fig. 3a, the purity of NEs reached 97 % after 6 h stimulation, higher than 4 h of 88.9 %, hence 6 h after the thioglycollate broth injection was chosen for subsequent NEs collection. Afterwards, DTNB/Fe(III)@BNP were loaded onto the NEs surface through the exchange of thiols on the cell membrane with disulfides of thiol-activated DTNB/Fe(III)@BNP to obtain the biomimetic nanoreactor. The CLSM images clearly indicated the fluorescent DTNB/Fe(III)@BNP was successfully attached onto the NEs cell surface (Fig. 3b), rendering the nanoreactor living delivery property. It is worth noting that the synthesis of biomimetic nanoreactor was conducted in a cytocompatible condition with high reaction efficiency (less than 10 min), which was essential to retain the biological functions of NEs for chemotactic migration. The cell surface loading of DTNB/Fe(III)@BNP was also characterized with scanning electronic microscope which exhibited relatively smooth interfacial architecture post the nanoreactor attachment (Fig. S9). To further validate the presence of DTNB/Fe(III)@BNP on the surface of NEs, NEs with or without nanoreactor loading were subjected to SDS-PAGE after DTT treatment. Compared with NEs, distinct aggregates were observed at the top of the band in nanoreactor

loading group (Fig. S10), which could be attributed to the unload and incomplete dissociation of DTNB/Fe(III)@BNP from NEs surface. These results together demonstrated the successful loading of nanoreactor onto the surface of NEs.

To verify the effect of surface loading on main biological functions of NEs, DTNB/Fe(III)@BNP with different concentrations (0.1 mg mL^{-1}, 0.2 mg mL^{-1} and 0.3 mg mL^{-1}) was employed to incubate with the NEs. The fluorescence intensity gradually increased with elevated treatment concentrations, implying the successful loading of DTNB/Fe(III)@BNP (Fig. 3c). CD11b, a specific membrane protein associated with NEs, plays vital roles in regulating the adhesion and migration towards inflammation. As shown in Fig. 3d, negligible difference was measured in CD11b level of NEs incubated with different concentrations of DTNB/Fe(III)@BNP, indicating the well retained chemotaxis after the drug loading. No obvious morphological change was perceived after the attachment of DTNB/Fe(III)@BNP onto NEs surface (Fig. 3e). Cell viability exerts prerequisite roles on biological functions, hence the viability of DTNB/Fe(III)@BNP-NEs was measured using apoptosis assay. There were no apparent difference in viable cell population with over 85 % proportion (Fig. 3f), indicating the favorable cytocompatibility of the loading process. Collectively, these results demonstrated that the nanoreactor could be efficiently loaded onto the NEs surface through rapid thiol-disulfide exchange and the loading process imposed little effect on the biological functions of NEs, indicating the great promise for cargo delivery.
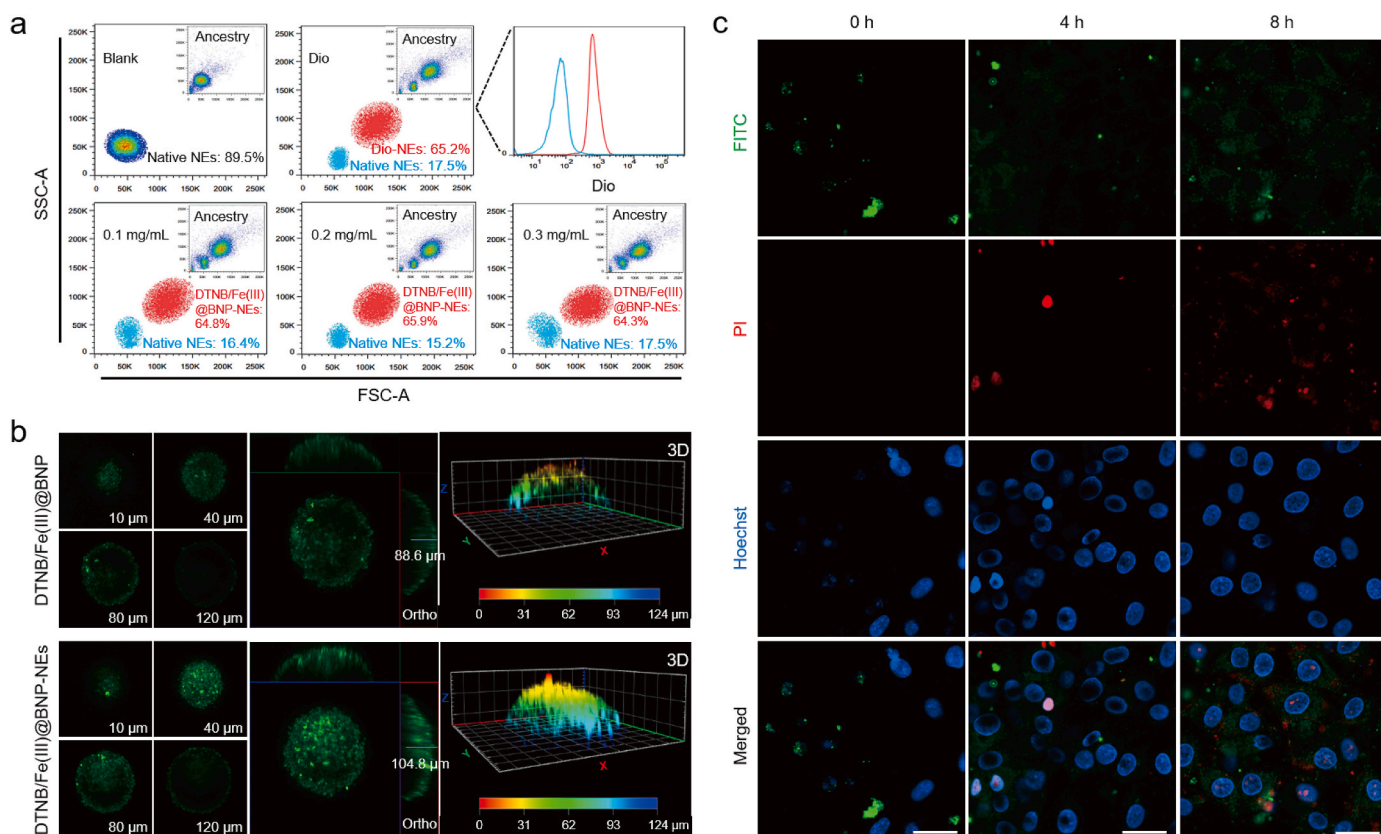

Fig. 4. Inflammation-primed targeted delivery. (a) Flow analysis of NEs isolated from peritoneal cavity after the intravenous administration of FITC-labeled DTNB/Fe(III)@BNP-NEs prepared at different DTNB/Fe(III)@BNP concentrations. Dio-labeled NEs were also administrated and used as control. Referring to the blank control, the blue population could be gated as the native NEs, while the red population could be attributed to FITC-labeled DTNB/Fe(III)@BNP-NEs or Dio-labeled NEs, based on the distinction in fluorescence intensity. (b) Penetration of FITC-labeled DTNB/Fe(III)@BNP or DTNB/Fe(III)@BNP-NEs into the 3D C6 tumor spheroids after incubation for 4 h. CLSM images were collected with a Z-stack thickness of 30–40 μm in hemisphere. (c) CLSM images of C6 cells incubated with DTNB/Fe(III)@BNP-NEs for different times. The liberated DNA segments were stained with PI, and the nuclei of C6 cells was stained with Hoechst. Scale bar, 20 μm.

2.1. Inflammation-primed targeted delivery to tumor

To investigate the inflammation mediated chemotactic migration of the biomimetic nanoreactor, an *in vivo* recruitment experiment was carried out according to the collection of NEs. As exhibited in Fig. 4a and Fig. S11, the collected NEs from peritoneal cavity upon stimulation with thioglycollate broth after FITC-labeled DTNB/Fe(III)@BNP-NEs administration could be divided into two populations. The blue population was presumed to the autologous NEs based on the absence of fluorescence signal, referred to the blank group, while the red population could be ascribed to the injected DTNB/Fe(III)@BNP-NEs since obvious fluorescence was detected. Interestingly, negligible difference was found in the migration proportion of NEs treated with various DTNB/Fe(III)@BNP concentrations, which was comparable to that of Dio-labeled NEs. The results suggested that the attachment of DTNB/Fe(III)@BNP on cell surface barely affected the chemotactic migration of NEs toward inflamed site for brain targeting. Given the superior drug loading capacity, biomimetic nanoreactor prepared at 0.3 mg mL^{-1} DTNB/Fe(III)@BNP was chosen for subsequent experiment.

The tumor-penetration capability of DTNB/Fe(III)@BNP-NEs was assessed employing a three-dimensional (3D) multicellular tumor spheroid model. After incubation with FITC-labeled DTNB/Fe(III)@BNP or DTNB/Fe(III)@BNP-NEs, the fluorescence signal was detected from the surface to the central region of the tumor spheroid with 120 μm depth. As shown in Fig. 4b, the FITC fluorescence of DTNB/Fe(III)@BNP-NEs group was clearly observed at 80 μm depth and distributed in most areas of the tumor after 4 h treatment. In contrast, FITC signal was visualized mainly on the periphery and only feeble fluorescence

presented at 40 μm depth of the tumor spheroid incubated with DTNB/Fe(III)@BNP. The results demonstrated that the penetration capability of NEs was well retained after the surface loading of DTNB/Fe(III)@BNP.

We next evaluated the inflammation-primed intercellular trafficking of cargo from NEs to tumor cells (Fig. 4c). To simulate the inflammatory stimuli of tumor, the supernatant after tumor cell culture for 24 h was collected and utilized for the dispersion of DTNB/Fe(III)@BNP-NEs. When FITC-labeled DTNB/Fe(III)@BNP-NEs were initially introduced to the C6 monolayer, the FITC and Hoechst of tumor nuclei fluorescence were clearly observed in separated form, whereas PI signal was not detected. After 4 h incubation, DTNB/Fe(III)@BNP-NEs unloaded DTNB/Fe(III)@BNP, accompanied by the formation of neutrophil extracellular traps (NETs) indicated by PI fluorescence, implying the dissociation of NEs being over-activated. As time extended to 8 h, a large number of unloaded DTNB/Fe(III)@BNP was endocytosed by C6 cells as evidenced by the colocalization of FTIC and Hoechst in the same tumor cell, which subsequently exerted favorable cytotoxicity (Fig. S12). Accordingly, NEs could unload the surface attached nanoreactor in response to the inflammation stimuli, which was later endocytosed by tumor cells and produce abundant ·OH for cell killing.

***In Vivo* Biodistribution and Brain-Tumor Targeting.** The *in vivo* biodistribution of nanoreactor surface attached onto NEs was conducted in a C6 glioma model employing the *In Vivo* Imaging System. Cy7-labeled DTNB/Fe(III)@BNP was incubated with NEs to prepare the fluorescent DTNB/Fe(III)@BNP-NEs. As shown in Fig. 5a and Fig. S13, DTNB/Fe(III)@BNP-NEs efficiently targeted to the inflamed brain tumor, as evidenced by the strong fluorescence in tumor at 1 h post the
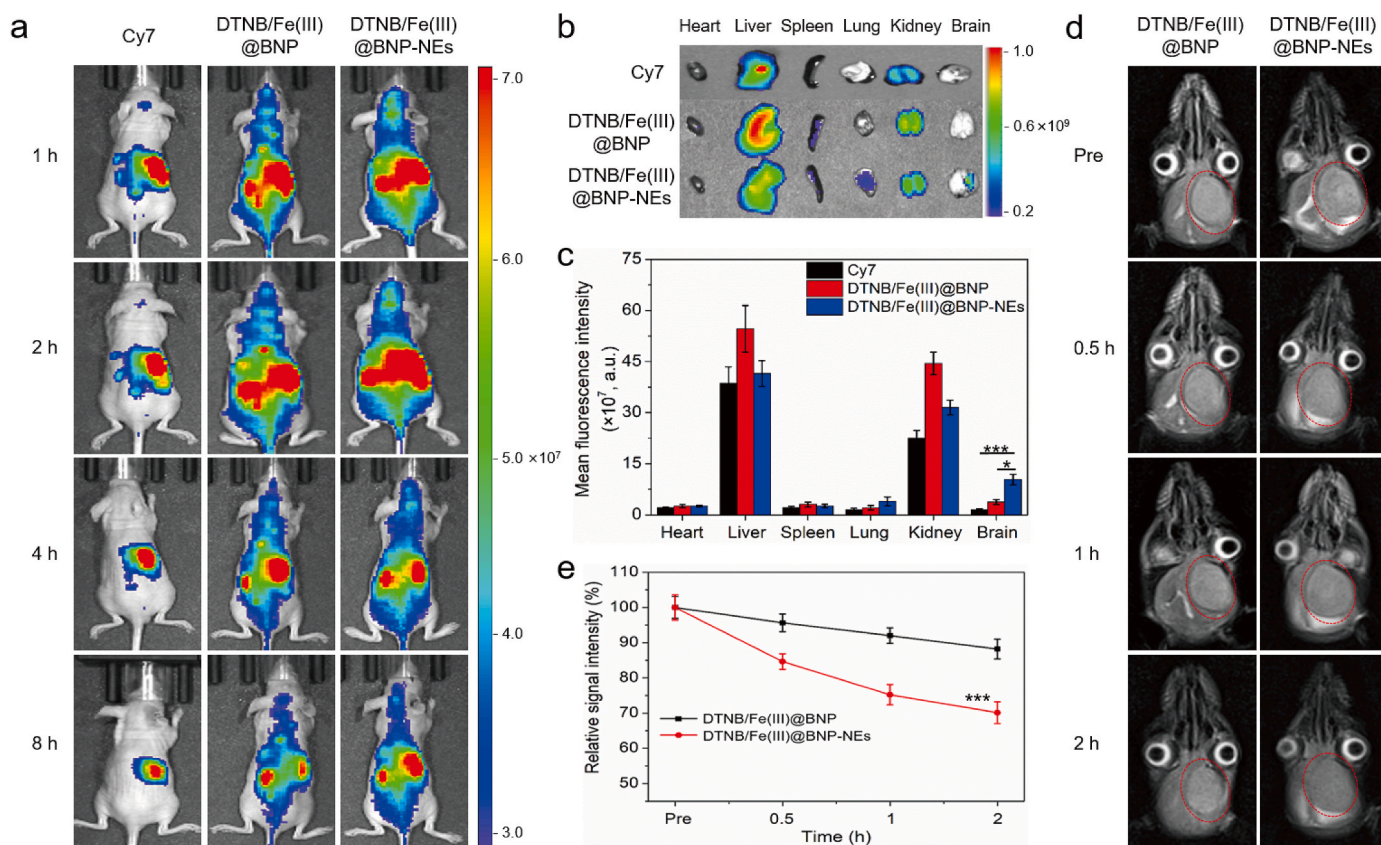

Fig. 5. *In vivo* biodistribution and brain-tumor targeting. (a) Fluorescence images of C6-bearing mice intravenously administrated with Cy7, Cy7-labeled DTNB/Fe(III)@BNP or DTNB/Fe(III)@BNP-NEs at indicated time points. (b) Fluorescence images of major organs excised from mice at 2 h post the administration of Cy7, Cy7-labeled DTNB/Fe(III)@BNP or DTNB/Fe(III)@BNP-NEs. (c) Quantitative analysis of mean fluorescence intensity in organs at 2 h post administration. Data are shown as mean ± s.d. ($n = 3$). *$P < 0.05$, ***$P < 0.001$. (d) T_2-weighted MR images of C6-bearing mice pre and post injection of DTNB/Fe(III)@BNP or DTNB/Fe(III)@BNP-NEs. The red circles indicate the tumor region. (e) Relative signal intensity of C6 glioma versus time post administration. Data are shown as mean ± s.d. ($n = 3$). ***$P < 0.001$.

intravenous administration. The accumulation of DTNB/Fe(III)@BNP-NEs in tumor reached the summit peak at 2 h and then suffered a gradual decrease in the next 6 h. During the whole observation period, much stronger fluorescence was monitored at the inflamed brain tumor from mice administrated with DTNB/Fe(III)@BNP-NEs than that of mice injected with DTNB/Fe(III)@BNP or Cy7 dye. To investigate the biodistribution of the three formulations, the major organs were excised and imaged at 2 h post injection (Fig. 5b). The results showed that Cy7 or DTNB/Fe(III)@BNP mainly distributed in the liver and kidney, the two specialized organs for drug metabolism. In contrast, the accumulation of DTNB/Fe(III)@BNP-NEs in the two metabolic organs obviously decreased, while significantly increased deposition was observed in the brain, which was further verified by CLSM imaging of excised brain tissues (Fig. S14). The statistical analysis indicated a nearly threefold increase in fluorescence intensity of brain tumor compared with mice administrated with DTNB/Fe(III)@BNP group (Fig. 5c), revealing the inflammation-primed boosted brain-tumor targeting of the biomimetic nanoreactor.

The vectorization of DTNB/Fe(III)@BNP-NEs to the inflamed brain tumor was further assessed using T_2-weighted MR imaging. Compared with the DTNB/Fe(III)@BNP group, mice administrated with DTNB/Fe(III)@BNP-NEs exhibited stronger contrast enhancement of negative signals in the brain tumor site (Fig. 5d). The effect of contrast enhancement was further calculated based on the signal intensity. As presented in Fig. 5e, the relative signal intensity of DTNB/Fe(III)@BNP-NEs decreased by nearly 20 % in 2 h compared to that of DTNB/Fe(III)@BNP group. The results further validated the chemotactic migration of NEs in response to the inflamed brain tumor, favorable for the brain-tumor targeted delivery of surface attached cargoes.

***In Vivo* Therapeutic Effect.** To evaluate the therapeutic effect, C6-bearing mice were randomly divided into four groups and intravenously administrated with PBS, NEs alone, DTNB/Fe(III)@BNP or DTNB/Fe(III)@BNP-NEs. Then by using the *In Vivo* Imaging System, the tumor volume was imaged and the bioluminescence intensity was quantitatively analyzed. At the meantime, survival time of mice in each treatment group was recorded and the survival curve was plotted. As shown in Fig. 6a–c and Fig. S15, the brain tumor in each group exhibited similar bioluminescence intensity at the initial of therapy. Besides, there was no apparent difference in signal intensity monitored between PBS and NEs groups in the overall treatment period. However, mice administrated with DTNB/Fe(III)@BNP-NEs efficiently inhibited the glioma progression, enabling the maximum survival time extended from 23 d to 32 d compared with PBS group. These results suggested that DTNB/Fe(III)@BNP could be targeted delivered to brain tumor with the assistance of NEs in respond to inflammation chemotaxis, which later exerted enhanced CDT efficacy due to the efficient regulation of Fenton chemistry.

We further performed histological analysis of glioma-bearing mice brains after the various treatment (Fig. 6d). HE staining revealed dense glioma cells typically representing malignancy in both PBS and NEs groups, in which masses of Ki67 positive cells were observed, indicating the well-retained proliferation capability after the treatment. In comparison, the cell density and Ki67 expression obviously decreased in DTNB/Fe(III)@BNP-NEs treated mice, indicating that DTNB/Fe(III)@BNP-NEs could effectively inhibit the tumor propagation. HE staining were also carried out in various organs excised from mice in each group (Fig. S16), and no apparent histological changes were observed. For further toxicity assessment, healthy mice were administrated with DTNB/Fe(III)@BNP or DTNB/Fe(III)@BNP-NEs, and their weight change and blood chemistry were measured. The body weight of mice suffered a gradual increase regardless of the drug administration (Fig. S17). Moreover, the levels of blood urea nitrogen (BUN) and creatinine (CRE) as well as alanine transaminase (ALT) and aspartate transaminase (AST), important indicators of kidney and hepatic function respectively, exhibited no significant difference in the blood of healthy mice (Table S2). These results collaboratively demonstrated the biosafety of DTNB/Fe(III)@BNP-NEs for antitumor application.

3. Conclusions

We have developed a tailored biomimetic nanoreactor to potentiate glioma CDT efficacy through synchronous GSH exhaustion and acidity elevation. DTNB was utilized to drive the disulfide-based nanoassembly of BSA molecules, along which Fenton agent Fe(III) was encapsulated, the resultant nanoreactor DTNB/Fe(III)@BNP was thus prepared with triple GSH depletion and prompt acidity elevation properties favorable for the occurrence of intratumoral Fenton reaction. Moreover, loading the nanoreactor onto the cell surface via disulfide-thiol exchange negligibly influenced the biological function of NEs, enabling the inflammation-primed targeted delivery of the biomimetic nanoreactor
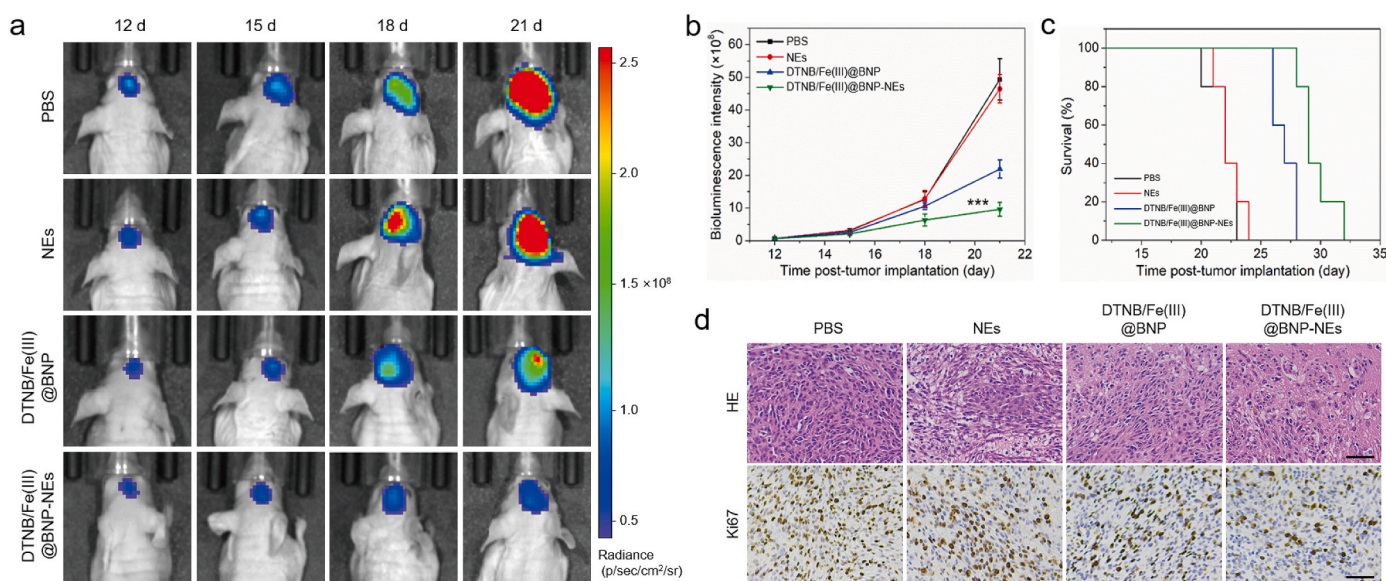

Fig. 6. *In vivo* therapeutic performance. (a) *Iv vivo* bioluminescent images, (b) quantitative bioluminescence intensity and (c) survival curves of C6-bearing mice after the indicated treatment. Data are shown as mean ± s.d. (*n* = 5). ***P < 0.001 (compared with the PBS group). (d) The hematoxylin and eosin (HE) and Ki67 staining of C6 glioma-bearing mouse brain after the various treatments. Scale bar, 50 μm.

for therapeutic purpose. Importantly, retarded glioma progression and improved survival rate were demonstrated in the glioma mouse models undergoing DTNB/Fe(III)@BNP-NEs treatment, suggesting that DTNB/Fe(III)@BNP hijacked by NEs could efficiently accumulate in the inflamed tumor site and drive the occurrence of Fenton reaction to maximize the antitumor efficacy. This work presents a novel CDT strategy based on the targeted exhaustive and synchronous regulation of Fenton chemistry for alternative glioma therapy.

CRediT authorship contribution statement

Ya Wen: Writing – original draft, Investigation, Data curation. **Qiansai Qiu:** Visualization, Methodology. **Feng Feng:** Writing – review & editing, Conceptualization. **Yujuan Zhu:** Writing – review & editing, Methodology. **Jianquan Zhang:** Visualization, Methodology. **Zesheng Sun:** Methodology, Investigation. **Tuodi Zhang:** Writing – review & editing. **Wei Shi:** Writing – review & editing, Conceptualization. **Jinlong Shi:** Writing – review & editing, Funding acquisition, Conceptualization.

Declaration of competing interest

The authors declare that they have no known competing financial interests or personal relationships that could have appeared to influence the work reported in this paper.

Acknowledgements

Appendix A. Supplementary data

Supplementary data to this article can be found online at https://doi.org/10.1016/j.mtbio.2025.101447.

Data availability

Data will be made available on request.

References

[1] Z. Tang, Y. Liu, M. He, W. Bu, Chemodynamic therapy: tumour microenvironment-mediated Fenton and fenton-like reactions, Angew Chem. Int. Ed. Engl. 58 (4) (2019) 946–956, https://doi.org/10.1002/anie.201805664.

[2] X. Wei, R. Han, Y. Gao, P. Song, Z. Guo, Y. Hou, J. Yu, K. Tang, Boosting energy deprivation by synchronous interventions of glycolysis and oxidative phosphorylation for bioenergetic therapy synergetic with chemodynamic/photothermal therapy, Adv. Sci. (2024) 2401738, https://doi.org/10.1002/advs.202401738.

[3] X. Li, B. Ding, J. Li, D. Han, H. Chen, J. Tan, Q. Meng, P. Zheng, P.a. Ma, J. Lin, Valence-tailored copper-based nanoparticles for enhanced chemodynamic therapy through prolonged ROS generation and potentiated GSH depletion, Nano Res. (2024), https://doi.org/10.1007/s12274-024-6552-2.

[4] J. Chen, X. Wang, Y. Zhang, S. Zhang, H. Liu, J. Zhang, H. Feng, B. Li, X. Wu, Y. Gao, B. Yang, A redox-triggered C-centered free radicals nanogenerator for self-enhanced magnetic resonance imaging and chemodynamic therapy, Biomaterials 266 (2021) 120457, https://doi.org/10.1016/j.biomaterials.2020.120457.

[5] Y. Zhou, S. Fan, L. Feng, X. Huang, X. Chen, Manipulating intratumoral Fenton chemistry for enhanced chemodynamic and chemodynamic-synergized multimodal therapy, Adv Mater 33 (2021) 2104223, https://doi.org/10.1002/adma.202104223.

[6] Y. Wang, L. Shi, Z. Ye, K. Guan, L. Teng, J. Wu, X. Yin, G. Song, X.B. Zhang, Reactive oxygen correlated chemiluminescent imaging of a semiconducting polymer nanoplatform for monitoring chemodynamic therapy, Nano Lett. 20 (1) (2020) 176–183, https://doi.org/10.1021/acs.nanolett.9b03556.

[7] X. Chen, H. Zhang, M. Zhang, P. Zhao, R. Song, T. Gong, Y. Liu, X. He, K. Zhao, W. Bu, Amorphous Fe-based nanoagents for self-enhanced chemodynamic therapy by Re-establishing tumor acidosis, Adv. Funct. Mater. 30 (6) (2020) 1908365, https://doi.org/10.1002/adfm.201908365.

[8] S. Wilhelm, A.J. Tavares, Q. Dai, S. Ohta, J. Audet, H.F. Dvorak, W.C.W. Chan, Analysis of nanoparticle delivery to tumours, Nat. Rev. Mater. 1 (5) (2016) 16014, https://doi.org/10.1038/natrevmats.2016.14.

[9] M. Wu, H. Zhang, C. Tie, C. Yan, Z. Deng, Q. Wan, X. Liu, F. Yan, H. Zheng, MR imaging tracking of inflammation-activatable engineered neutrophils for targeted therapy of surgically treated glioma, Nat. Commun. 9 (2018) 4777, https://doi.org/10.1038/s41467-018-07250-6.

[10] Y. Xiong, C. Xiao, Z. Li, X. Yang, Engineering nanomedicine for glutathione depletion-augmented cancer therapy, Chem. Soc. Rev. 50 (10) (2021) 6013–6041, https://doi.org/10.1039/d0cs00718h.

[11] P. Liu, L. Hao, M. Liu, S. Hu, Glutathione-responsive and -exhausting metal nanomedicines for robust synergistic cancer therapy, Front. Bioeng. Biotechnol. 11 (2023) 1161472, https://doi.org/10.3389/fbioe.2023.1161472.

[12] D. Han, B. Ding, P. Zheng, M. Yuan, Y. Bian, H. Chen, M. Wang, M. Chang, A.A. Al Kheraif, P.a. Ma, J. Lin, NADPH oxidase-like nanozyme for high-efficiency tumor therapy through increasing glutathione consumption and blocking glutathione regeneration, Adv Healthc Mater (2024) 2303309, https://doi.org/10.1002/adhm.202303309.

[13] B. Niu, K. Liao, Y. Zhou, T. Wen, G. Quan, X. Pan, C. Wu, Application of glutathione depletion in cancer therapy: enhanced ROS-based therapy, ferroptosis, and chemotherapy, Biomaterials 277 (2021) 121110, https://doi.org/10.1016/j.biomaterials.2021.121110.

[14] L.-S. Lin, J. Song, L. Song, K. Ke, Y. Liu, Z. Zhou, Z. Shen, J. Li, Z. Yang, W. Tang, G. Niu, H.-H. Yang, X. Chen, Simultaneous fenton-like ion delivery and glutathione depletion by MnO2-based nanoagent to enhance chemodynamic therapy, Angew Chem. Int. Ed. Engl. 57 (18) (2018) 4902–4906, https://doi.org/10.1002/anie.201712027.

[15] Y. Huang, Y. Jiang, Z. Xiao, Y. Shen, L. Huang, X. Xu, G. Wei, C. Xu, C. Zhao, Three birds with one stone: a ferric pyrophosphate based nanoagent for synergetic NIR-triggered photo/chemodynamic therapy with glutathione depletion, Chem Eng J 380 (2020) 122369, https://doi.org/10.1016/j.cej.2019.122369.

[16] X. Wang, X. Zhong, Z. Liu, L. Cheng, Recent progress of chemodynamic therapy-induced combination cancer therapy, Nano Today 35 (2020) 100946, https://doi.org/10.1016/j.nantod.2020.100946.

[17] S. Fassi, K. Djebbar, I. Bousnoubra, H. Chenini, T. Sehili, Oxidation of bromocresol green by different advanced oxidation processes: Fenton, Fenton-like, photo-Fenton, photo-Fenton-like and solar light. Comparative study, Desalin Water Treat 52 (25–27) (2014) 4982–4989, https://doi.org/10.1080/19443994.2013.809971.

[18] Y. Kato, S. Ozawa, C. Miyamoto, Y. Maehata, A. Suzuki, T. Maeda, Y. Baba, Acidic extracellular microenvironment and cancer, Cancer Cell Int. 13 (2013) 89, https://doi.org/10.1186/1475-2867-13-89.

[19] S. Dong, Y. Dong, T. Jia, F. Zhang, Z. Wang, L. Feng, Q. Sun, S. Gai, P. Yang, Sequential catalytic, magnetic targeting nanoplatform for synergistic photothermal and NIR-enhanced chemodynamic therapy, Chem. Mater. 32 (23) (2020) 9868–9881, https://doi.org/10.1021/acs.chemmater.9b05170.

[20] W. Zhao, J. Hu, W. Gao, Glucose oxidase-polymer nanogels for synergistic cancer-starving and oxidation therapy, ACS Appl. Mater. Interfaces 9 (28) (2017) 23528–23535, https://doi.org/10.1021/acsami.7b06814.

[21] X. Zhang, C. He, Y. Chen, C. Chen, R. Yan, T. Fan, Y. Gai, T. Yang, Y. Lu, G. Xiang, Cyclic reactions-mediated self-supply of H2O2 and O2 for cooperative chemodynamic/starvation cancer therapy, Biomaterials 275 (2021) 120987, https://doi.org/10.1016/j.biomaterials.2021.120987.

[22] P. Swietach, R.D. Vaughan-Jones, A.L. Harris, Regulation of tumor pH and the role of carbonic anhydrase 9, Cancer Metast Rev 26 (2) (2007) 299–310, https://doi.org/10.1007/s10555-007-9064-0.

[23] J. Xue, Z. Zhao, L. Zhang, L. Xue, S. Shen, Y. Wen, Z. Wei, L. Wang, L. Kong, H. Sun, Q. Ping, R. Mo, C. Zhang, Neutrophil-mediated anticancer drug delivery for suppression of postoperative malignant glioma recurrence, Nat. Nanotechnol. 12 (7) (2017) 692–700, https://doi.org/10.1038/nnano.2017.54.

[24] E.V. Batrakova, H.E. Gendelman, A.V. Kabanov, Cell-mediated drug delivery, Expert Opin Drug Deliv 8 (4) (2011) 415–433, https://doi.org/10.1517/17425247.2011.559457.

[25] C. Zhang, L. Zhang, W. Wu, F. Gao, R.Q. Li, W. Song, Z.N. Zhuang, C.J. Liu, X.Z. Zhang, Artificial super neutrophils for inflammation targeting and HClO generation against tumors and infections, Adv Mater 31 (19) (2019) e1901179, https://doi.org/10.1002/adma.201901179.

[26] L. Yang, Y. Zhang, Y. Zhang, Y. Xu, Y. Li, Z. Xie, H. Wang, Y. Lin, Q. Lin, T. Gong, X. Sun, Z. Zhang, L. Zhang, Live macrophage-delivered doxorubicin-loaded liposomes effectively treat triple-negative breast cancer, ACS Nano 16 (6) (2022) 9799–9809, https://doi.org/10.1021/acsnano.2c03573.

[27] A.C. Wan, J.Y. Ying, Nanomaterials for in situ cell delivery and tissue regeneration, Adv. Drug Deliv. Rev. 62 (7–8) (2010) 731–740, https://doi.org/10.1016/j.addr.2010.02.002.

[28] M.R. Choi, K.J. Stanton-Maxey, J.K. Stanley, C.S. Levin, R. Bardhan, D. Akin, S. Badve, J. Sturgis, J.P. Robinson, R. Bashir, N.J. Halas, S.E. Clare, A cellular Trojan horse for delivery of therapeutic nanoparticles into tumors, Nano Lett. 7 (12) (2007) 3759–3765, https://doi.org/10.1021/nl072209h.

[29] A.C. Anselmo, S. Mitragotri, Cell-mediated delivery of nanoparticles: taking advantage of circulatory cells to target nanoparticles, J Control Release 190 (2014) 531–541, https://doi.org/10.1016/j.jconrel.2014.03.050.

[30] J.K. Lee, I.S. Choi, T.I. Oh, E. Lee, Cell-surface engineering for advanced cell therapy, Chemistry 24 (59) (2018) 15725–15743, https://doi.org/10.1002/chem.201801710.

[31] J. Park, J. Andrade, Y. Seo, M.J. Kim, S.C. Zimmerman, H. Kong, Engineering the surface of therapeutic "living" cells, Chem Rev 118 (4) (2018) 1664–1690, https://doi.org/10.1021/acs.chemrev.7b00157.

[32] Y. Wen, Y. Liu, F. Guo, Y. Han, Q. Qiu, Y. Li, H. Dong, T. Ren, Y. Li, A vaccine for photodynamic immunogenic cell death: tumor cell caged by cellular disulfide-thiol exchange for immunotherapy, Biomater. Sci. 9 (3) (2021) 973–984, https://doi.org/10.1039/d0bm01393e.

[33] Q. Qiu, Y. Wen, H. Dong, A. Shen, X. Zheng, Y. Li, F. Feng, A highly sensitive living probe derived from nanoparticle-remodeled neutrophils for precision tumor imaging diagnosis, Biomater. Sci. 7 (12) (2019) 5211–5220, https://doi.org/10.1039/c9bm01083a.

[34] X. Meng, J. Deng, F. Liu, T. Guo, M. Liu, P. Dai, A. Fan, Z. Wang, Y. Zhao, Triggered all-active metal organic framework: ferroptosis machinery contributes to the apoptotic photodynamic antitumor therapy, Nano Lett. 19 (11) (2019) 7866–7876, https://doi.org/10.1021/acs.nanolett.9b02904.